High Stress Drop and Slow Rupture During the 2020 MW6.4 Intraplate Petrinja Earthquake, Croatia

Iva Zilic, Mathieu Causse, Martin Vallée, Snježana Markušić

HAL Id: hal-04892942

https://hal.science/hal-04892942v1

Submitted on 17 Jan 2025

JGR Solid Earth

Key Points:

- We present the first kinematic model of the 2020 M_w6.4 Petrinja earthquake
- The stress drop was high (∼25 MPa) and the rupture propagated slowly (speed of ∼0.5V_s)
- The large stress drop may have contributed to boost energy dissipation and slow down rupture along this immature fault system

Supporting Information:

Supporting Information may be found in the online version of this article.

Correspondence to:

I. Žilić,
iva.zilic@gfz.hr

Author Contributions:

Conceptualization: Mathieu Causse
Data curation: Iva Žilić, Mathieu Causse, Snježana Markušić
Formal analysis: Iva Žilić, Mathieu Causse, Martin Vallée
Funding acquisition: Snježana Markušić
Investigation: Mathieu Causse
Methodology: Iva Žilić, Mathieu Causse, Martin Vallée
Project administration: Snježana Markušić
Software: Iva Žilić, Mathieu Causse
Supervision: Mathieu Causse
Validation: Mathieu Causse
Visualization: Iva Žilić, Mathieu Causse
Writing – original draft: Iva Žilić, Mathieu Causse
Writing – review & editing: Iva Žilić, Mathieu Causse

High Stress Drop and Slow Rupture During the 2020 MW6.4 Intraplate Petrinja Earthquake, Croatia

Iva Žilić[1] , Mathieu Causse[2] , Martin Vallée[3], and Snježana Markušić[1]

[1]Department of Geophysics, Faculty of Science, University of Zagreb, Zagreb, Croatia, [2]Université Grenoble-Alpes, Université Savoie Mont Blanc, CNRS, IRD, UGE, ISTerre, Grenoble, France, [3]Institut de Physique du Globe de Paris, CNRS, Paris, France

Abstract Here we analyze the rupture process of the 29 December 2020 M_W6.4 Petrinja earthquake (Croatia), the largest event instrumentally recorded in this area characterized by a moderate strain-rate intraplate setting. We use foreshocks and aftershocks, recorded at more than 80 broadband stations located 70–420 km from the earthquake, as empirical Green's functions (EGFs) to separate source effects from propagation and local site effects. First, we deconvolve the mainshock P-wave time windows from the EGFs in the frequency domain to obtain the corner frequency (f_c). Spectral analysis based on the Brune's source model reveals a large stress drop of 24 MPa. Next, by deconvolving the Love waves in the time domain, we calculate the Apparent Source Time Functions (ASTFs). We find that the average duration of the source is ∼5 s, with no significant directivity effects, indicating a bilateral rupture. To extract physical rupture parameters such as rupture velocity, slip distribution and rise time, we deploy two techniques: (a) Bayesian inversion and (b) backprojection onto isochrones of ASTFs. Both techniques show a low rupture velocity (40%–50% of the shear wave velocity) and a rupture length of less than 10 km, that is, much less than would typically be expected for a magnitude 6.4 earthquake. This apparent anticorrelation between stress drop and rupture velocity may be attributed to the complex and segmented fault system characteristic of immature intraplate settings.

Plain Language Summary Source and ground motion features of intraplate earthquakes are still poorly understood, due to relatively low seismicity rates and generally sparse station distribution. Here we analyze the rupture properties of the 2020 M_W6.4 Petrinja (Croatia) intraplate earthquake, the largest event instrumentally recorded in this area. The Petrinja earthquake occurred in a moderate-seismicity area on a poorly characterized fault system, which remained relatively silent since the 1909 M_L5.8 Kupa Valley earthquake, that Andrija Mohorovičić used for his discovery of the Mohorovičić Discontinuity (MOHO). We use foreshocks and aftershocks, recorded at more than 80 broadband stations located 70–420 km from the earthquake, to separate source effects of the mainshock from propagation and local site effects and obtain a model of the rupture. The results indicate a slow rupture propagation (speed of 40%–50% of the shear wave velocity). In addition, the rupture length of less than 10 km, that is, much less than would typically be expected for a magnitude 6.4 earthquake, is in agreement with the large inferred stress drop. Such particular properties could be fairly current in immature intraplate settings, which has some direct impact on seismic hazard.

1. Introduction

The Croatian territory, situated at the convergence of three significant geological units—the Alps to the northwest, the Pannonian basin to the east, and the Dinarides to the south (Ustaszewski et al., 2008)—exhibits a moderate level of seismic activity, occasionally experiencing strong earthquakes ($M > 6$). Most earthquakes in this area stem from strain accumulation driven by the Adria microplate's rotation toward the Eurasian tectonic plate (Anderson & Jackson, 1987; Battaglia et al., 2004; Calais et al., 2002; Ustaszewski et al., 2010). The Croatian Earthquake Catalogue (CEC), updated and first described in Herak et al. (1996), documents over 150 earthquakes with a magnitude greater than 5, that occurred in Croatia or the neighboring countries in the last 100 years.

In terms of seismic activity, year 2020 was critical for Croatia and Croatian people, with the occurrence of two destructive earthquakes: the M_L5.5 Zagreb event on the 22nd of March and the M_W6.4 Petrinja event on the 29th of December. These events occurred approximately 70 km apart, both resulting in human casualties and extensive damage. This study focuses on the 2020 Petrinja earthquake, one of the most powerful recorded events in the wider region, surpassing the expected magnitude for this area (Markušić et al., 2021). This area holds particular

significance as it was the location of the 1909 M_L 5.8 Kupa Valley earthquake, that Andrija Mohorovičić used for his discovery of the Mohorovičić Discontinuity (MOHO) between the Earth's crust and mantle (Herak & Herak, 2010).

In the early morning, at 6:28 local time on 28 December 2020, a moderate M_L 5.0 earthquake, the first foreshock of the sequence, struck the broader Petrinja area. In the next 29 hr, this event was followed by 38 additional foreshocks, including a significant M_L 4.7 earthquake occurring less than two hours after the initial one. The subsequent day, on December 29th at 12:19, the powerful M_W 6.4 mainshock struck the region. The epicentral intensity reached VIII-IX °EMS indicating its destructive power. The earthquake was felt in a radius of at least 400 km, with reports of people sensing the shaking in Croatia, Bosnia and Herzegovina, Slovenia, Serbia, Austria, Hungary, Italy, and even Czechia (Markušić et al., 2021). Seven people lost their lives, dozens were injured, and thousands remained homeless because of the extensive damage of towns and villages close to the epicenter (such as Sisak, Petrinja, Glina, Majske Poljane, etc.; Miranda et al., 2021). Furthermore, the intense ground shaking led to secondary destructive effects such as liquefaction of underground sinkholes, particularly in the vicinity of Mečenčani village. There, over a hundred sinkholes collapsed, including one with a diameter exceeding 20 m (Baize et al., 2022; Markušić et al., 2021).

The M_W 6.4 Petrinja mainshock occurred in a moderate strain-rate intraplate setting on the complex Petrinja-Pokupsko fault system (Baize et al., 2022; Xiong et al., 2021). Source and ground motion features of intraplate earthquakes are still poorly understood, due to relatively low seismicity rates and sparse station distribution (e.g., Onwuemeka et al., 2018; Viegas et al., 2010). This further underscores the significance of a comprehensive and meticulous analysis of the seismic source and its impact on ground shaking for enhancing future seismic hazard assessments.

In this study, our primary aim is to determine the rupture process of the M_W 6.4 Petrinja mainshock. We first use seismological data located at distances between 70 and 420 km to obtain Apparent Source Time Functions (ASTFs) in the framework of a point source model, both in the frequency and time domain. The ASTFs are next inverted within a Bayesian framework, to obtain stress drop and kinematic source parameters, including the effective dimensions of rupture, the distribution of final slip, rupture velocity, rise time, and the associated uncertainties. We also deploy an alternative technique, referred to as backprojection of ASTFs. We next discuss the inferred rupture properties in light of the tectonic setting. Given the absence of near-fault strong motion recordings in the observed area, the obtained kinematic rupture model provides us source parameters necessary for subsequent near-fault strong motion simulations. This is an important issue for improving seismic hazard assessment in the region but also more generally in moderate strain-rate intraplate environments.

2. Seismological Data

To constrain the mainshock source parameters, we use seismological data (see section Data availability) recorded at 83 stations all over Italy, Slovenia, Austria, Slovakia, Hungary, Croatia, Bosnia and Hercegovina, and Montenegro, which results in a good azimuthal coverage (Figure 1). As will be detailed subsequently, seismograms are deconvolved from wave propagation effects both in the frequency domain (stations indicated with blue triangles) and in the time domain (stations indicated with yellow triangles). We use data from stations at epicentral distances ranging from approximately 70–420 km. First, we resampled the higher rate stations (100 and 200 Hz) to a consistent 50 Hz rate of the majority of the Croatian records. Further, we band-pass filtered all data between 0.01 and 20 Hz. We exclusively utilize data with a signal-to-noise ratio exceeding 2, a point that will be elaborated upon later.

2.1. Empirical Green's Function Analysis

To analyze the behavior of an earthquake source, it is necessary to isolate the source effect from the seismic waveform recorded at the seismic station. An earthquake seismogram, *s(t)*, results from the convolution of earthquake source effects *e(t)*, propagation and local site effects *G(t)*, and the known instrument response *I(t)*:

$$s(t) = e(t) * G(t) * I(t). \tag{1}$$

When we aim to isolate source effects alone, the concept of empirical Green's function (EGF) analysis comes into play. This method is founded on the assumption that suitable foreshocks or aftershocks, which can be used as
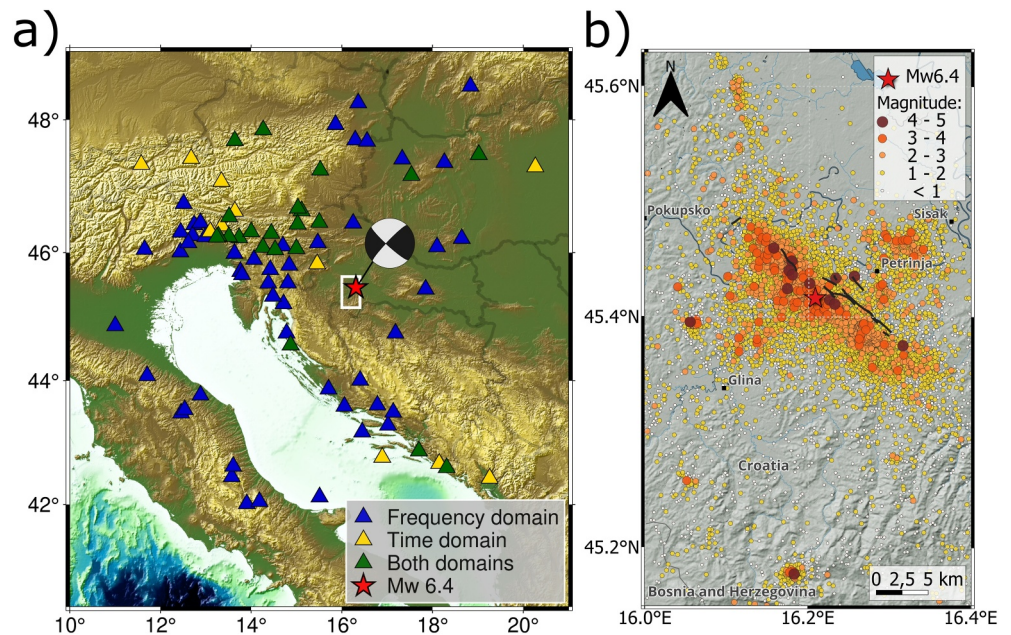
Figure 1. Station distribution and Petrinja earthquake sequence. (a) The color of the triangles indicates the type of analysis for which each station has been used (frequency domain or time-domain deconvolution). The red star shows the epicenter of the mainshock and the corresponding focal mechanism ($\phi = 132°$, $\delta = 79°$, $\lambda = 170°$). The area indicated with a white rectangle is zoomed in on (b); (b) Epicenters of Petrinja earthquake sequence displaying events between 28 December 2020, and 31 December 2021. Black lines represent co-seismic rupture trace (Baize et al., 2022).

EGFs, efficiently model propagation and local site effects. It has been widely used to analyze earthquake source processes (e.g., Abercrombie, 2021; Hartzell et al., 1978; Pennington et al., 2022; Uchide & Song, 2018). According to Lay and Wallace (1995), an earthquake preceding or following the mainshock can serve as an EGF if it meets the following criteria: (a) it exhibits an almost identical focal mechanism as the mainshock; (b) the hypocentral depth closely matches that of the mainshock; (c) the earthquake magnitude is high enough to provide a satisfactory Signal-to-Noise Ratio (*SNR*) but simultaneously low enough to minimize the influence of its own source effects compared to the mainshock. To satisfy the last condition, it is preferable to have an earthquake with a magnitude at least two units smaller than the one of the mainshock.

In this study, we consider six earthquakes as potential EGF candidates (Table 1) with magnitudes exceeding 4. The events in Table 1 were relocated using the latest version of the HYPOSEARCH software, which calculates hypocentral coordinates and origin times based on P- and S-wave arrival times, with depth uncertainties estimated at ±1 km (Herak, 1989) and a modified crustal model from B.C.I.S. (1972). Focal mechanisms of the EGF candidate earthquakes listed in Table 1 are reported by GFZ (GEOFON project, https://geofon.gfz-potsdam.de/eqinfo/; last accessed: 2024 September 23). We have first checked that the selected EGFs have coefficients of correlation with the mainshock exceeding 0.7. Among these six observed earthquakes, EGF2 emerges as the optimal candidate, and it is subsequently utilized in our research.

Our analysis of the source process is divided into three steps: (a) Frequency domain EGF deconvolution, in which we compute corner frequency as a function of azimuth, and compute stress drop assuming a circular crack model; (b) Time-domain EGF deconvolution, to infer ASTFs, representing the source time function "seen" from a seismic station (e.g., Chounet et al., 2018; Mueller, 1985); (c) Lastly, we present a kinematic source model obtained using kinematic inversion and backprojection of the ASTFs.

2.2. Frequency Domain EGF Deconvolution

Frequency domain EGF deconvolution provides insights into stress drop and potential directivity effects (e.g., Abercrombie, 2021; Abercrombie et al., 2016; Holmgren et al., 2019; Kane et al., 2011; Shearer et al., 2019). Here we mostly follow the procedure described in Abercrombie et al. (2016).

Table 1
The Mainshock and Earthquakes Considered as Potential Empirical Green's Function Candidates

Event label	Date	Time (UTC)	Position (°N, °E)	Depth (km)	M_W	Focal mechanism	ϕ [°], δ [°], λ [°]
Mainshock	29.12.2020.	11:19	45.401, 16.200	8	6.4		**NP1: 132, 79, 170** NP2: 224, 80, 12
EGF1	09.01.2021.	21:29	45.413, 16.217	8	4.2		**NP1: 140, 89, −163** NP2: 50, 73, 0
EGF2	06.01.2021.	17:01	45.412, 16.206	9	4.7		**NP1: 138, 80, −177** NP2: 48, 87, −9
EGF3	30.12.2020.	05:26	45.442, 16.179	7	4.6		**NP1: 345, 65, −179** NP2: 255, 89, −24
EGF4	30.12.2020.	05:15	45.439, 16.167	9	4.8		**NP1: 144, 81, −175** NP2: 53, 85, −8
EGF5	28.12.2020.	06:49	45.424, 16.236	10	4.6		**NP1: 144, 86, −170** NP2: 53, 80, −3
EGF6	28.12.2020.	05:28	45.369, 16.351	9	5.1		**NP1: 327, 88, 164** NP2: 57, 74, 1

Note. Nodal plains (NP) in agreement with geological data are bolded.

First, we manually select body waves from the recordings. We perform the analysis on both P and S waves. Nevertheless, the analysis is supposed to be more robust using P waves because they are easier to pick and it is difficult for most stations to separate S waves from Love waves. Hereafter the analysis is presented for P waves only. The results for S waves are shown in Figure S1 in Supporting Information S1. We use a time-window length of $nsec = 30$ s, as proposed by Abercrombie et al. (2016) for such a magnitude. For the closest stations, for which $T_S - T_P < 30$ s, $nsec$ is chosen equal to $T_S - T_P$. Using a Butterworth filter, we then initially bandpass filter our data within the range of $f_{min} = 1/nsec$ and $f_{max} = 5$ Hz. This step is crucial for fitting the Brune's spectrum to the P-wave spectra.

We select only frequencies of the *P*-wave spectra with a signal-to-noise ratio (*SNR*) greater than 2. Additionally, we cross-correlate EGF events waveforms with those of the mainshock, retaining only those with cross-correlation above 0.7 (Abercrombie et al., 2016). We perform this using EGF2, EGF5, and EGF6, but, as mentioned, focus on results obtained using EGF2 waveforms. Since it is not expected that the mainshock and the EGF candidate correlate well at frequencies above the corner frequency of the stronger event (Abercrombie, 2015), the P windows are bandpass filtered between $1/nsec$ and 0.2 Hz before computing cross-correlation. This step is to ensure proper alignment and accurate cross-correlation. We tested various cross–

correlation threshold values (0.4–0.8) to compromise good azimuthal coverage with more stations and data quality.

After isolating the *P*-wave windows of the mainshock and well-correlated EGFs, we compute displacement and Fourier spectra. We approximate the source process with a "ω^{-2} model" (Aki, 1967; Brune, 1970) assuming that an earthquake can be represented by a circular crack in an elastic medium (Brune, 1970). Subsequently, to calculate the corner frequencies, we conduct Brune's spectrum fitting on averaged spectral ratio for each station. The theoretical spectral ratio has the following form:

$$\frac{\dot{M}_1(f)}{\dot{M}_2(f)} = \frac{M_{01}}{M_{02}} \left(\frac{1 + (f/f_{c2})^{\gamma n}}{1 + (f/f_{c1})^{\gamma n}} \right)^{1/\gamma}. \tag{2}$$

In Equation 2, *f* represents frequency, f_{c1} and f_{c2} are the corner frequencies for the mainshock and EGF earthquakes, with the seismic moments of M_{01} and M_{02} respectively. *n* is a factor representing high-frequency fall-off assumed as $n = 2$, and γ controls the shape of the corner, which we set to a value $\gamma = 1$ based on Brune (1970). Before fitting, the spectra obtained at each station individually from all EGF recordings and components are stacked. Despite the differences in magnitude among the EGFs, spectral stacking enhances the signal-to-noise ratio and averages out individual biases. This approach therefore reduces uncertainties and results in less biased outcomes compared to individually fitting each spectral ratio (Abercrombie, 2016; Kane, 2011). We then perform Brune's spectrum fitting using grid search following Viegas et al. (2010) to obtain corner frequencies of the mainshock and the EGF, f_{c1} and f_{c2}, respectively. For the grid search we use frequency step of 0.01 Hz in the range 0.03–5 Hz. To quantify uncertainties, we perform Bayesian estimates of the model parameters as proposed in Causse et al. (2021). Figure 2a illustrates the whole process for station VENJ of the Croatian network and displays Joint Probability Density Functions of the parameters f_{c1} and f_{c2}. Note that we only use f_{c1}, which is much better resolved than the EGF corner frequency f_{c2}.

With knowledge of seismic moment, corner frequency, and assuming a simple circular source model, we can compute stress drop using Equation 3 (e.g., Brune, 1970; Eshelby, 1957):

$$\Delta\sigma = \frac{7M_0}{16} \frac{f_c^3}{k^3\beta^3} \tag{3}$$

Focusing on *P*-waves, the *k* value equals 0.32 (e.g., Madariaga, 1976), and we use a shear wave velocity (β) of 3,400 m/s, a velocity value around a focal depth of both target and EGF events based on the Balkan model (B.C.I.S., 1972). The assumed depth of the mainshock is around 8 km as shown in Table 1.

We calculate corner frequencies for each station and compute the mean values for azimuthal classes with 45° intervals (Figure 2c). Subsequently, we compare the obtained azimuthal variations of the corner frequencies with the values obtained for a line source model assuming unilateral or bilateral rupture scenarios (see Text S1 in Supporting Information S1) to investigate the overall rupture behavior. The comparison indicates weak azimuthal variations of the corner frequency, which is consistent with a bilateral rupture.

Additionally, using the same Madariaga (1976) source model we calculate an average corner frequency (f_c) value of 0.24 Hz, obtained by fitting the spectral ratio stacking over all stations. From Equation 3, this gives a stress drop of 24 MPa. Considering the standard deviation on f_c values (Figure 2c), the 95%-confidence interval is [5 MPa, 84 MPa]. Note that we run the procedure for various values of *nsec* and cross-correlation thresholds. For instance, using *nsec* = 20 s gives a stress drop of 27 MPa. Furthermore, using a cross-correlation threshold of 0.8 results in a stress drop of 20 MPa. Finally, the stress drop value obtained using S waves equals 65 MPa (Figure S1 in Supporting Information S1). Despite this uncertainty, our analysis indicates a large stress drop value, as will be discussed subsequently (Section 4).

2.3. Time-Domain EGF Deconvolution

The next step involves computing ASTFs using the EGF method. ASTFs represent the moment rate functions observed at each station. Though ASTFs were primarily derived using body waves from mainshocks and smaller events (e.g., Mueller, 1985), we use surface waves due to their dominance in the waveforms and superior
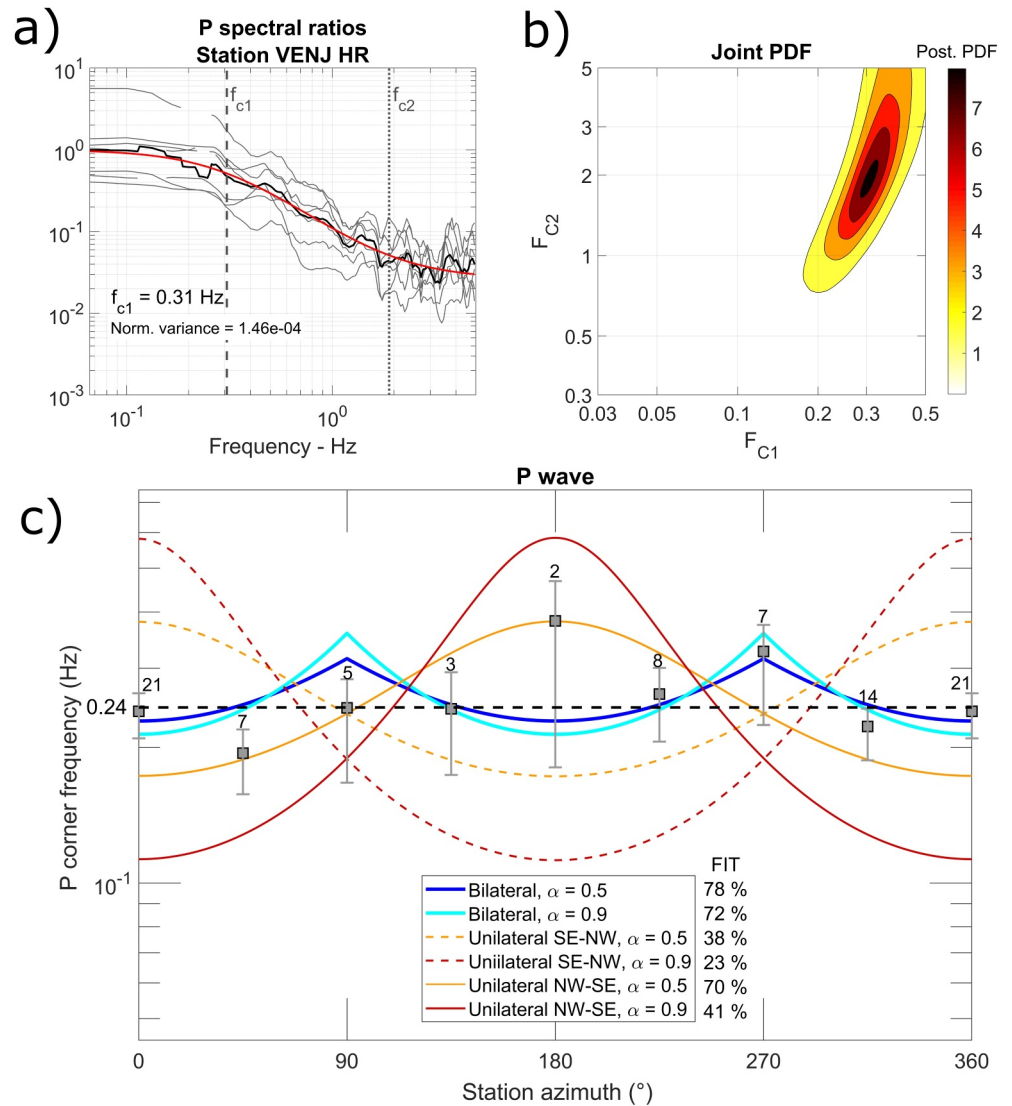
Figure 2. Corner frequency determination. (a) Ratios between mainshock and empirical Green's functions (EGFs) *P*-wave spectra used for f_c computation at Venje (Croatia) station. The black curve represents the average and the red curve the best-fitting model. The calculated corner frequencies f_{c1} and f_{c2} values are shown respectively by gray dashed and dotted vertical lines; (b) Joint Probability Density Function of the mainshock and EGF corner frequency at Venje (Croatia) station (F_{C1} and F_{C2} respectively); (c) Computed f_c values from seismic data, relative to the station azimuth, compared to theoretical values for a line source model with unilateral and bilateral ruptures, indicating the level of fit and corresponding f_c error bars (see Text S1 in Supporting Information S1). The azimuth is relative to the direction N310°, so that it equals 0° along the fault to the northwest. The black horizontal dashed line represents the average f_c value over all stations and all the assumed EGFs. α represents the ratio between the rupture velocity and the *P*-wave velocity. For each azimuthal class, the gray square represents the mean corner frequency value. Numbers on the error bars indicate the number of used stations in the given station azimuth range. The value of the takeoff angle is assumed to be ~48° (the mean takeoff angle value over all used stations).

signal-to-noise ratios. In addition, body waves in the considered distance range are composed of various regional phases, which are difficult to separate, introducing potential instability in the deconvolution process. Here we focus on Love waves, which are dominant for the nearly vertical strike-slip rupture of the Petrinja mainshock. As Love waves propagate horizontally, they accentuate azimuthal variations of ASTFs contributing to better resolution of kinematic rupture parameters. Finally, the horizontal propagation eliminates potential biases associated with uncertainties in body waves take-off angles in obtaining a finite source model from ASTFs (Section 3). Hereafter the time-deconvolution methodology is then presented for Love waves only. ASTFs obtained using P
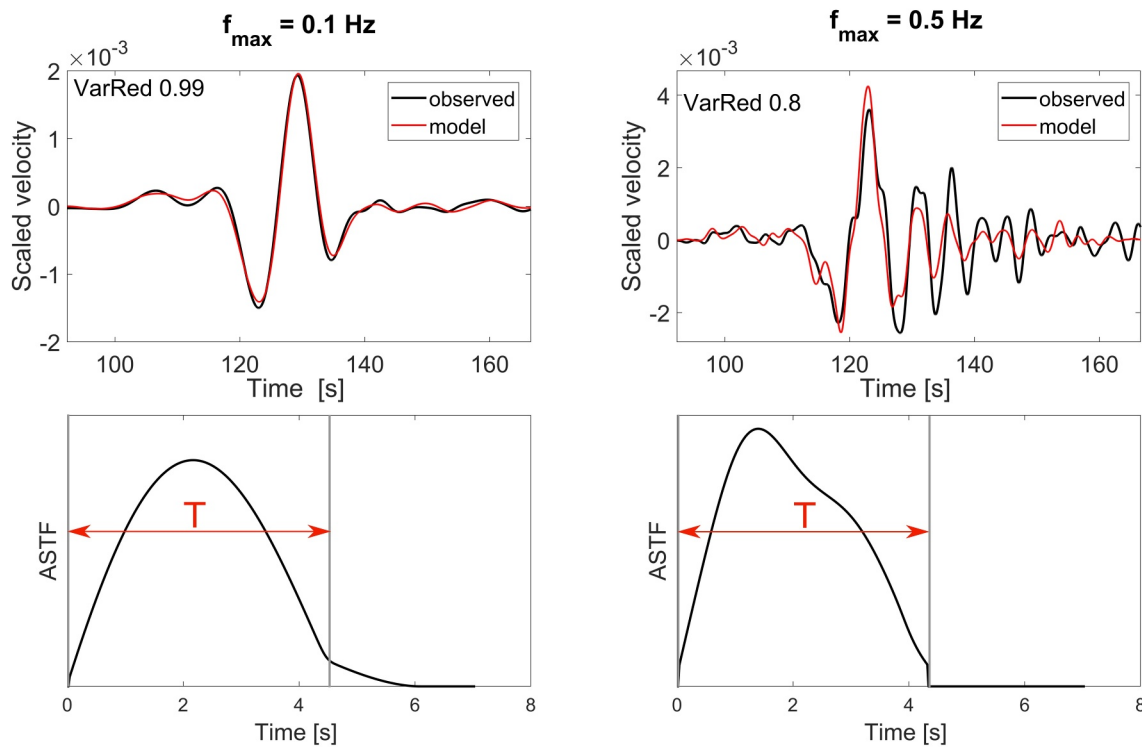
Figure 3. Results of the empirical Green's function (EGF) deconvolution process at PDG station. Comparison between simulated and observed data are shown in the top panel and obtained Apparent Source Time Functions (ASTFs) are shown in the bottom panel. In the bottom panel, the ASTF duration is indicated by the red arrow. It is calculated as the duration of the ASTF phase with amplitude level above 10% of the ASTF maximum value (Courboulex et al., 2016). Mainshock and EGF data have been lowpass filtered below $f_{max} = 0.1$ Hz (a) or $f_{max} = 0.5$ Hz (b). The ASTF amplitudes are normalized to their maximum value.

and S waves are provided as Supplementary Figures (Figures S2 and S3 in Supporting Information S1) and will not be used for the finite source modeling.

We thus use the transversal components of both main and EGF waveforms. We manually pick mainshock and EGF Love wave windows. Given the difficulty to accurately identify the Love wave arrival times, we start the mainshock window 1.5 s before the picked time. This process ensures that the obtained ASTFs are causal. To perform the deconvolution, we use the projected Landweber algorithm, imposing constraints of positivity, causality, and bounded duration of the ASTFs (Bertero et al., 1997; Vallée, 2004). We measure the level of fit as $(1 - misfit) \times 100\%$, where $misfit$ is the ratio between the Euclidean norm of the residuals and of the data. First, we conduct the deconvolution process on seismograms low-pass filtered at 0.1 Hz (Figure 3a), selecting only those stations for which the fit between observed and modeled waveforms exceeds 90%. Subsequently, we repeat this process for the selected stations but using a low-pass filter at 0.5 Hz (Figure 3b) and retaining ASTFs with a fit level above 60%. After obtaining the ASTFs for each station, we manually align them and suppress non-physical features. This involves removing values below 10% of the maximum ASTF value, as well as eliminating isolated bumps and ASTFs showing abnormally elongated or irregular shapes suggestive of non-physical slow rupture initiation or termination in the source (Figure S6 in Supporting Information S1).

The ASTF duration is measured as the ASTF span from its initial amplitude exceeding 0.1 times the peak value (Fm) to the final amplitude above 0.1 times Fm (Courboulex et al., 2016). Note that the ASTFs obtained from deconvolution of seismograms lowpass filtered at 0.1 Hz have minimum durations of 4 s and therefore still have energy at frequencies larger than 0.1 Hz. This arises because the core of the deconvolution process is a spectral division between the mainshock and EGF, and both are lowpass filtered using the same filter. As such, lowpass filtering does not affect the resolution of the minimum ASTF duration (Figure S4 in Supporting Information S1). In addition, the signal-to-noise ration of both the EGF and the mainshock data are far above 10 in the frequency
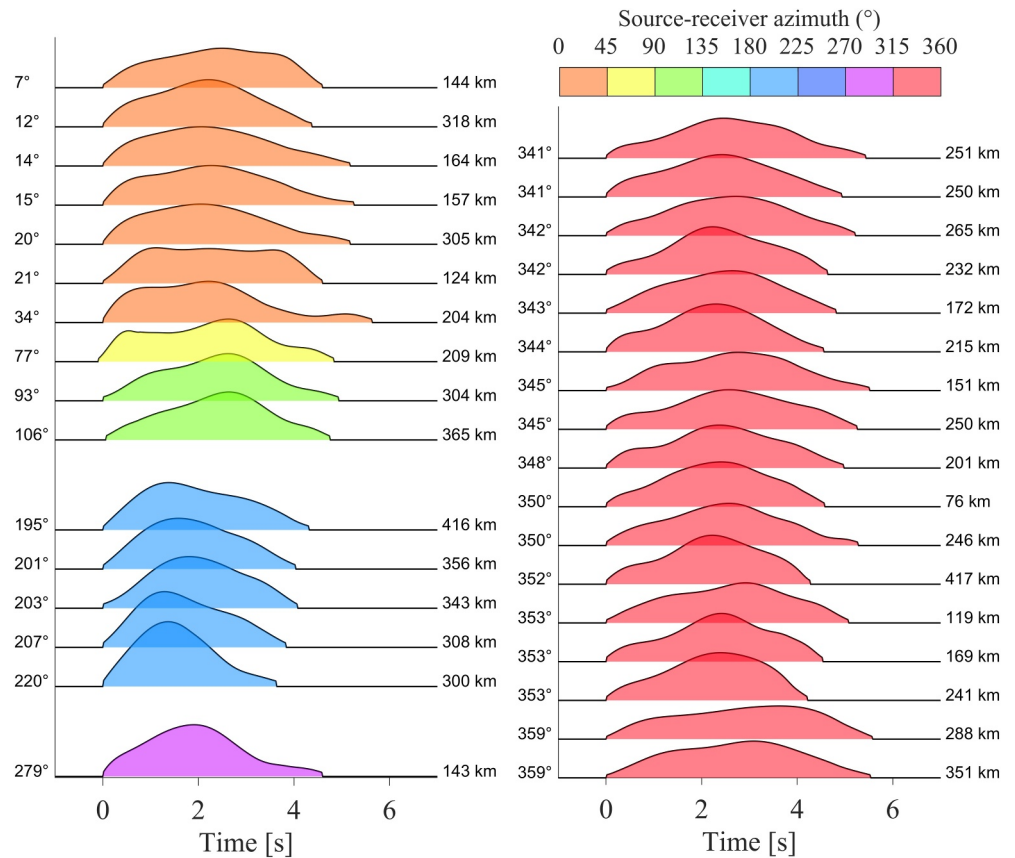
Figure 4. Apparent Source Time Functions (ASTFs) obtained from empirical Green's function deconvolution using Love waves low-pass filtered at $f_{max} = 0.5$ Hz. The ASTF amplitudes are normalized to their maximum value. The gaps on the left column represent present azimuthal gaps in the used data.

range 0.1–10 Hz, avoiding potential biases due to noise. Furthermore, the iterative deconvolution process aims to obtain ASTFs which, when convolved with the EGFs, fit the mainshock the time series. This explains why the resulting ASTFs are more complex when time series are lowpass filtered at 0.5 Hz than at 0.1 Hz, but still have the same duration (Figure 3).

To test the robustness of the inferred ASTFs, we perform the analysis using EGF2, EGF5, and EGF6 to obtain ASTFs and corresponding source durations (Figure S7 in Supporting Information S1). To characterize the uncertainty due to the use of various EGFs on the ASTFs duration, we compute the standard deviation of the natural logarithm residuals of duration, where logarithm residual for station i and each EGF j is defined as the absolute difference between the natural logarithm of the mean duration value and the natural logarithm of the duration obtained for each EGF ($\overline{ln(T_i)} - lnT_{i,j} \vee$). When considering all stations and all EGFs, we obtain a value of 0.08, indicating uncertainty of less than 10%. While the results show little dependence on the selected EGF, further analyses are conducted using EGF2, which provides the largest number of adequate ASTFs.

The above-described procedure results in 33 ASTFs. Despite some gaps in azimuthal coverage, especially between 135° and 180° of source-receiver azimuths due to limited station availability, we did not observe significant variability in source duration (Figure 4). Our results indicate ASTFs with rather abrupt termination and source durations between 4 and 6 s, with an average duration of 5 s. The average ASTF has similar amplitude and duration as the source function obtained from the SCARDEC method (Figure S5 in Supporting Information S1; Vallée and Douet (2016), http://scardec.projects.sismo.ipgp.fr/; last accessed: 2024 September 23), suggesting that the inferred ASTF durations are indeed not overestimated. A duration of 5 s is lower than the average expected value of approximately 8 s reported by Courboulex et al. (2016) for a $M_w6.4$ event
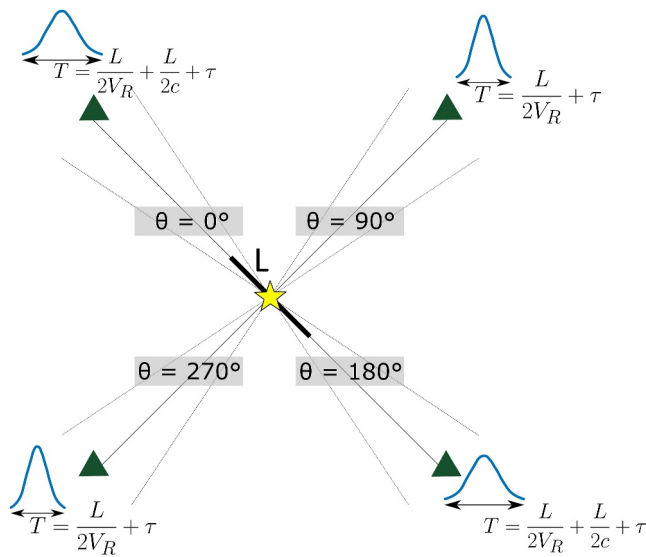
Figure 5. Theoretical value of the apparent source duration (T) for a line source rupturing bilaterally at rupture velocity V_R, for several source-receiver azimuths θ. τ represents the rise time.

(excluding subduction events). This is consistent with the study of Houston ([2001](#)), where shallow intraplate events show shorter durations and more abrupt source function terminations compared to events occurring in more active tectonic settings.

Note that EGF deconvolution provides ASTFs for the mainshock under the assumption that the EGF represents the impulse response of the medium. However, the real EGF duration is finite. Based on frequency domain deconvolution (Section [2.2](#)), EGF2 has corner frequency ranging between 1 and 1.5 Hz. Despite the large uncertainty on f_{c2}, this is consistent with an expected corner frequency in the range between 1 and 2 Hz for a M_W4.5 event (e.g., Abercrombie, [2021](#)). Source duration is related to corner frequency by $T = \alpha/fc$ with α between 1 and 1.7 s, depending on the source model (e.g., Courboulex et al., [2016](#)), which leads to an EGF duration between 0.3 and 1 s. Here we assume a duration of 0.7 s. Meng et al. ([2020](#)) used a time-domain stacking approach to account for variations in EGF duration and directivity effects. Here we assume a fixed mean EGF duration for simplicity. As will be shown subsequently (Section [3.1.3](#)), this choice is expected to have a minor impact on the inferred rupture parameters. We then correct the ASTFs by convolving them with a 0.7 s boxcar function, resulting with ASTFs of duration 0.7 s longer than shown in Figure [4](#). This set of corrected ASTFs is used in the following to obtain rupture parameters.

3. Finite Source Modeling

We deploy two different techniques to obtain a kinematic rupture models from the set of ASTFs. First, we use a Bayesian inversion technique. We next use an alternative method, called "isochrone backprojection," which provides faster estimates of the rupture parameters.

3.1. Bayesian Kinematic Inversion of ASTFs

We derive the 2020 Petrinja earthquake rupture model following a two-stage Bayesian inversion procedure detailed in Causse et al. ([2017](#)). ASTFs are inverted to obtain spatio-temporal rupture parameters, including mean rupture velocity, mean rise time, and slip distribution relative to the hypocenter. By aligning the slip distribution with independently analyzed epicentral location and hypocentral depth, we then establish the absolute slip distribution. The initial stage involves identifying the "best" rupture model (i.e., the maximum likelihood model). The second stage explores a range of "good" models (i.e., acceptable given the model uncertainty), from which uncertainty on the rupture parameters is quantified, including for instance trade-off between rupture parameters.

Figure [5](#) illustrates the expected tradeoffs between parameters in the case of a simple bilateral line source. Apparent source duration depends on rupture length (L), rupture velocity (V_R), and rise time (τ) for stations perpendicular to the rupture direction and depends also on phase velocity (c) for the other directions of observation. While a good azimuthal coverage combining seismological data recorded along and perpendicular to the fault can resolve L in bilateral ruptures, there is a trade-off between V_R and τ.

3.1.1. Inversion Procedure

We limit the fault dimensions to a length of 20,000 m and a width of 8,000 m, considering the shallow hypocentral depth (Baize et al., [2022](#)). We assume a subvertical fault with a strike of 130° and a dip of 84° and divide the fault plane into subfaults of 500 m × 500 m. At this stage, we assign equal weights to all data. Additionally, to convert seismic moment into slip, we use rigidity value as $\mu = 3.5 \times 10^{10}$ Pa. McGarr and Fletcher ([2003](#)) predict a maximum slip of ~2.5 m for a M_W6.4 event. To allow for potentially large slip, we set the maximum slip value to 6 m. As we anticipate lower resolution for V_R and τ, we consider relatively broad parameter ranges, with V_R between 800 m/s and 4,000 m/s and τ between 0.75 and 3 s (based on an expected average value of 1.5 s for a M_W6.4 earthquake with uncertainty factor of ~2, Gusev & Chebrov, [2019](#)). In addition, we use a Love wave phase velocity of 3,500 m/s (Text S3 and Figure S8 in Supporting Information [S1](#)). Finally, we keep the nucleation point position on the fault plane as a free parameter.
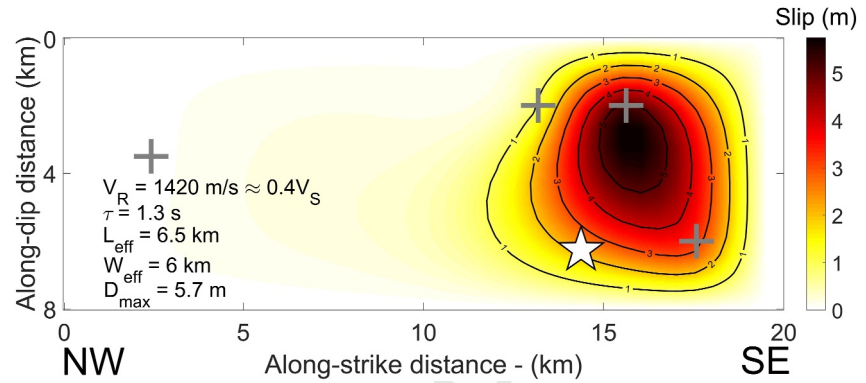
Figure 6. Finite source model obtained from Apparent Source Time Functions kinematic inversion for our preferred model. The color-scale depicts the final slip along the strike (NW–SE) and dip of the Pokupsko fault relative to the nucleation point represented by the white star. Gray crosses indicate the final locations of the four control points used to define the slip distribution.

In this study, we adopt the concept of a self-adapting grid (e.g., Causse et al., 2017; Hallo & Gallovič, 2020). The slip values are then not inverted on a regular grid of points but at a few control points, whose location is also inverted. The chosen number of these points enables us to control the spatial complexity actually required by the data. After obtaining slip values at these control points, the overall slip is interpolated over the fault plane using spline interpolation, setting slip to zero on the fault edges. Here, four control points are used. We have tested that using more control points does not improve the ASTF fit. Note that our inversion code can also identify potential variations of rupture velocity by incorporating control points that define local rupture velocity. Nevertheless, we have checked that using up to 4 control points does not result in a better fit with ASTF (Text S4 and Table S1 in Supporting Information S1). In the following, we then assume constant rupture velocity. The rise time is also assumed to be constant over the fault plane.

To explore the model space, we employ a Markov chain using the Metropolis algorithm (Metropolis et al., 1953). This iterative approach is simply a random walk, in which the "bad" models are unlikely to be accepted (e.g., Causse et al., 2017). The likelihood function is assumed to be Gaussian:

$$f(d|m) = c \cdot exp \qquad (4)$$

where d and m represent the data and model space, respectively, g represents the forward model to generate ASTFs from the rupture parameters and σ is a scalar. During the walk, a new candidate m_i at iteration i is accepted if the ratio of the likelihood functions $p = f(d|m_i)/f(d|m_{i-1})$ returns a probability larger than a random number between 0 and 1. p is expressed as:

$$p = \frac{f(d|m_i)}{f(d|m_{i-1})} = exp \qquad (5)$$

so that the acceptance rate of new candidates decreases with decreasing values of σ.

In the initial stage, our aim is to find the global minimum of the cost function by using a simulated annealing cooling scheme (Kirkpatrick et al., 1983). This involves an exploration of the model space followed by a gradual reduction of the σ values. To obtain the maximum likelihood model (the so-called "best" model), we conducted 14,000 iterations (Figure S9 in Supporting Information S1).

3.1.2. Inversion Results

We use this inversion procedure together with ASTFs obtained with $f_{max} = 0.5$ Hz (Section 2.3) to obtain a source model. The best source model is depicted in Figure 6. The effective rupture length (L_{eff}) and effective rupture width (W_{eff}) are computed as the maximum dimensions in the along-strike and along-dip directions for which slip values exceed 1 m. The simulated ASTFs from our preferred model accurately describe the observed ASTFs, with
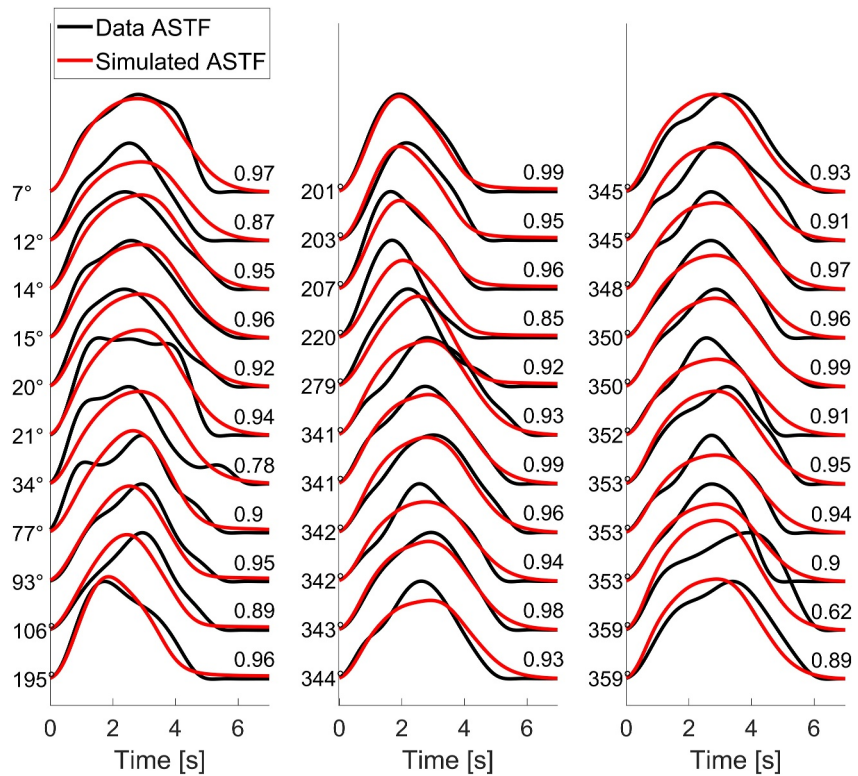
Figure 7. Comparison between Apparent Source Time Functions (ASTFs) obtained from Love waves lowpass filtered at $f_{max} = 0.5$ Hz (black) and simulated synthetic functions (red). The ASTF amplitudes are normalized to their maximum value. Source-to-station azimuths are indicated next to the left axis and the level of fit is indicated on the right side. The azimuth is 0° along the fault to the northwest.

a fit of 92%, computed as the mean value of the coefficient of determination R^2 over all stations (Figure 7, Text S4 and Table S1 in Supporting Information S1).

The best model indicates a slow rupture velocity ($\sim 0.4 V_S$), significant maximum slip value of about 5 m, and relatively small rupture dimensions. The slip patch, with slip values above 1 m, has an effective length of 6.5 km and an effective width of 6 km. Note that the procedure proposed by Somerville et al. (1999) to trim slip inversion models results in similar effective rupture dimensions. The slip patch is located above the nucleation point, resulting in predominantly upward rupture propagation, which is reported by Herak and Herak (2023) as well. The maximum slip area is however located slightly to the southeast of the nucleation, indicating a more southeast rupture propagation. Moreover, our obtained slip peaked approximately 3 km above the nucleation point and at an approximate depth of 4–5 km. For comparison, Herak and Herak (2023) reported an average slip patch of dimensions 5 km × 4 km located 4 km above the nucleation point with a peak slip of ~4 m based on the Kastelic et al. (2021) source model obtained from InSAR data. Xiong et al. (2022) also derived a source model using InSAR data suggesting an 8.33 km × 5.40 km slip patch with a maximum slip of 3.5 m. Interestingly, Henriquet et al. (2022) obtained a source model using a benchmark network combined with GNSS data describing a two-patch rupture 15 km long and 7 km wide. By its position and size, the slip patch of our best model mostly agrees with their deeper 7 km × 5 km slip patch despite its maximum slip being 3.5 m.

3.1.3. Uncertainty Analysis

Here we aim to derive the posterior distribution of the obtained kinematic parameters, representing a population of rupture models that all result in an acceptable fit with the data. Analyzing the acceptable model population offers insights into model resolution and potential parameter trade-offs. In this second stage, we use the results of the best model from the first stage as the initial parameter guess, exploring the model space starting from this point. The initial condition for the acceptable error (σ^2) is set as the cost value of the best model from the first stage. To
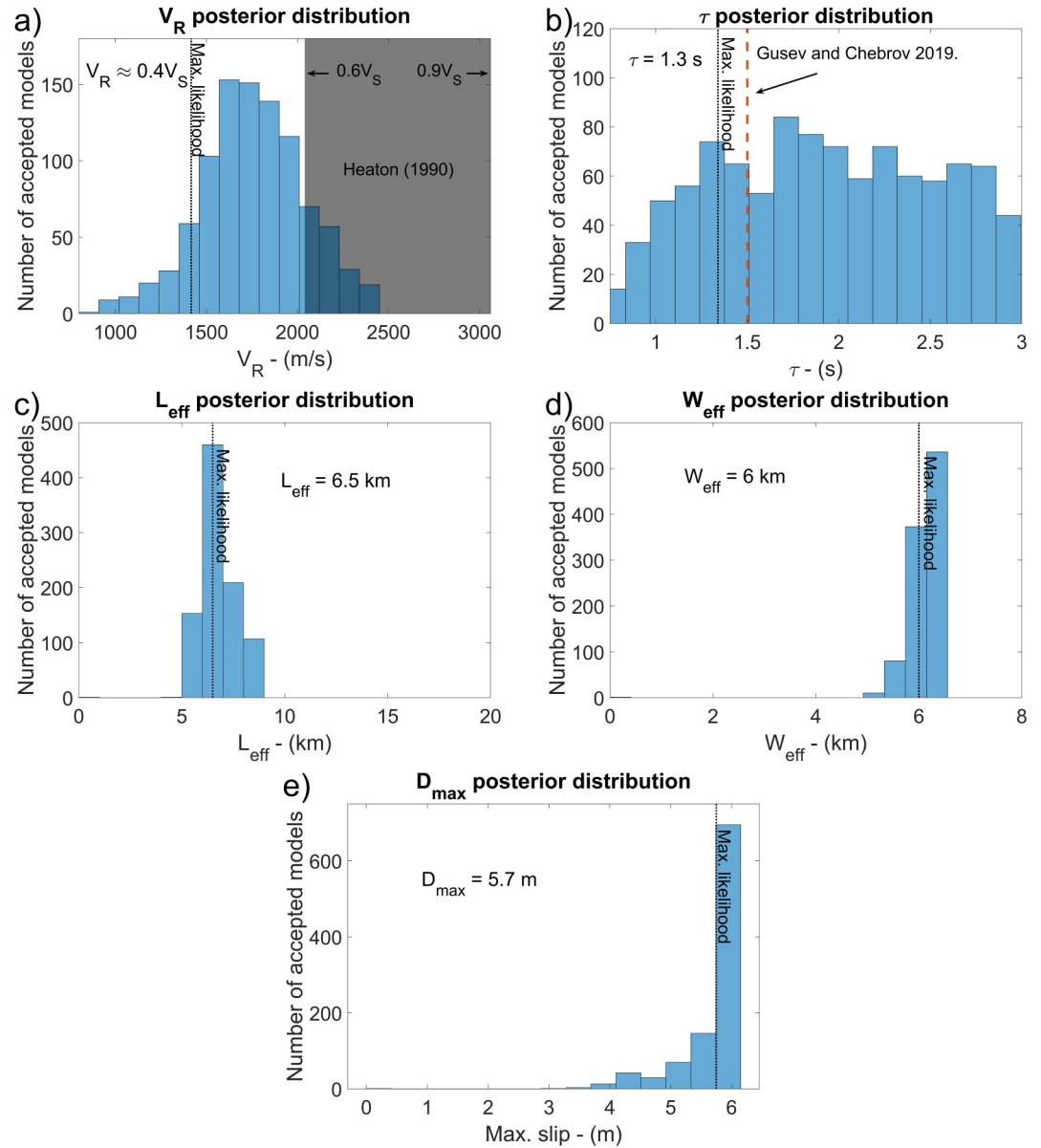
Figure 8. Posterior marginal distributions of obtained physical rupture parameters represented by histograms: (a) average rupture velocity (the gray area represents the range of values reported by Heaton (1990); (b) rise time (the dashed red line represents the median rise time value reported by Gusev and Chebrov (2019) for a $M_w6.4$ earthquake; (c) effective rupture length; (d) effective rupture width; (e) maximum slip. The maximum likelihood values are represented with the black dashed line.

mitigate the impact of uneven azimuthal coverage, σ^2 is determined as the squared median value of cost values for source-to-receiver azimuthal classes computed every $45°$. In this stage we perform 100,000 iterations, selecting every 100th sample to avoid autocorrelation, resulting in the 10,000 samples representing posterior distribution of kinematic source parameters (Figure 8).

From the posterior distributions we observe well-constrained rupture dimension and maximum slip, contrary to rupture velocity and rise time, which display expected uncertainties. The correlation matrix (Figure 9) illustrates the trade-off between rupture velocity (V_R) and rise time (τ), resulting in decreased resolution for V_R. Despite these trade-offs, the inversion suggests a slow rupture propagation ($V_R < 0.6 V_S$), where $V_S = 3,400$ m/s denotes the shear wave velocity at the rupture depth from the Balkan velocity model (B.C.I.S., 1972). The V_R values are approximately normally distributed with a mean of 1,790 m/s and a standard deviation of ~330 m/s. Moreover,
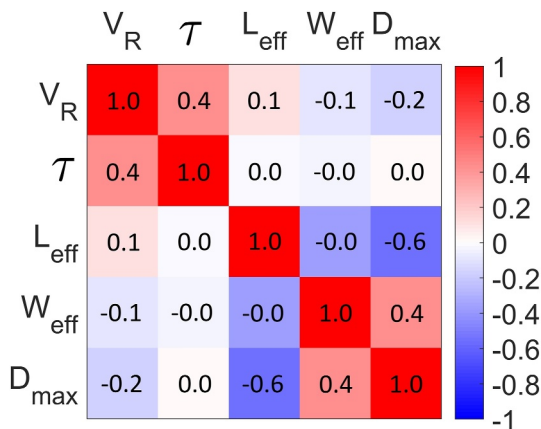
Figure 9. Correlation matrix of rupture parameters obtained from the Bayesian kinematic inversion.

the rise time is very poorly constrained. Note however that the value of 1.3 s obtained from the best model with maximum likelihood agrees with past earthquake analyses reporting an average rise time of ~1.5 s for a $M_W6.4$ earthquake (Gusev & Chebrov, 2019).

Additionally, we conducted several tests to assess the sensitivity of our model to the initial input parameters (Text S4 and Table S1 in Supporting Information S1). We inspected the impact of: (a) ASTF processing (original or convolved with a 0.7 s boxcar function as explained in Section 2.3, (b) low-pass filtering at 0.1 Hz or 0.5 Hz); (c) station weights; (d) fixed or free nucleation position; (e) increasing fault width to 12,000 m; (f) phase velocity values; (g) control points to account for rupture velocity variability over the fault plane. All tested scenarios indicate the same tendency as the best model: slow rupture velocity ($<0.6V_S$), relatively small slip patch, and significant maximum slip value.

3.2. Backprojection of ASTFs on Isochrones

We next use a method called "isochrone backprojection" to obtain the kinematic source parameters from the ASTFs (Király-Proag et al., 2019). The method provides fast estimates of the source parameters. It relies on the notion of isochrone, which represents the set of points on the fault that radiate seismic energy arriving at a given time t at a station (Figure S10 in Supporting Information S1). Since the seismic energy arrival time is the sum of the wave arrival time (Love wave in our case) and the rupture time, the computation of the isochrones requires a priori assumption on the rupture velocity and hypocenter position. Here, we assume a constant rupture velocity and a rupture initiation at 7.8 km hypocentral depth (Baize et al., 2021). The basic principle of the method is then to distribute the ASTFs observed at each station uniformly on its isochrones, at different time steps, thus providing the space-time evolution of seismic moment on the fault. It is important to note that the seismic moment release at a particular locus on the fault is spread out over the isochrones. As such the method provides a defocused image of the actual seismic moment release areas, the accuracy of which is defined by the intersection between the isochrone contributions of all stations (Festa & Zollo, 2006).

To improve focusing, we use an iterative procedure in which the residuals between ASTFs at iterations i and $i + 1$ are back-projected to obtain a new slip model (e.g., Beroza & Spudich, 1988). At the first iteration, the slip model obtained from back-projecting the original ASTFs is used to compute synthetic ASTFs. At the second iteration, the slip model obtained from the backprojection of the residuals, defined as the difference between original and synthetic ASTFs, is added to the slip model from the first iteration. The new slip model is used in turn to generate new ASTFs. The process is interrupted when the misfit - defined as the L2-norm between ASTFs at iterations i and $i + 1$—stops decreasing, within a limit of eight iterations. Since the procedure requires the reconstruction of synthetic ASTFs at each iteration, it also implies assuming a priori value of the rise time. The procedure is therefore run for various values of rupture velocity and rise time, and the rupture model with the minimum misfit is finally selected. The whole process is illustrated by synthetic tests, in which synthetic ASTFs are generated assuming three 4 km × 4 km slip patches at various depths (Figure 10). The results indicate that while the size and position of the slip patch located above the hypocenter is fairly well resolved (Figure 10a), the slip patches located at 5–10 km each side of the hypocenter are smeared along the fault dip (Figure 10b). Such a poor vertical resolution is inherent to the use of Love waves. It arises because isochrones beyond ~5 km from the hypocenter are predominantly vertical for horizontally propagating Love waves, whatever the source-station azimuth, resulting in a vertical smearing of the slip patches. The along-strike position of the slip patches remains, however, correct.

Figure 11 shows the obtained slip map for the $M_w6.4$ Petrinja earthquake, indicating a rupture length of roughly 10 km. The minimum misfit is obtained for a rupture velocity of 1,700 m/s ($\approx0.5V_S$) and a rise time of 0.5 s, which closely matches the results from the inversion (Figure 6 and Figure S11 in Supporting Information S1). By considering all parameters values resulting in a misfit smaller than 110% of the minimum misfit, we obtain that the rise time and the rupture velocity are in the range [0.5–1.5 s] and [1,300–1,900 m/s], respectively. The slip map corresponds to an approximately 10×8 km^2 slip patch located above the hypocenter. The obtained slip distribution compares fairly well to the slip obtained from kinematic inversion (Figure S11 in Supporting
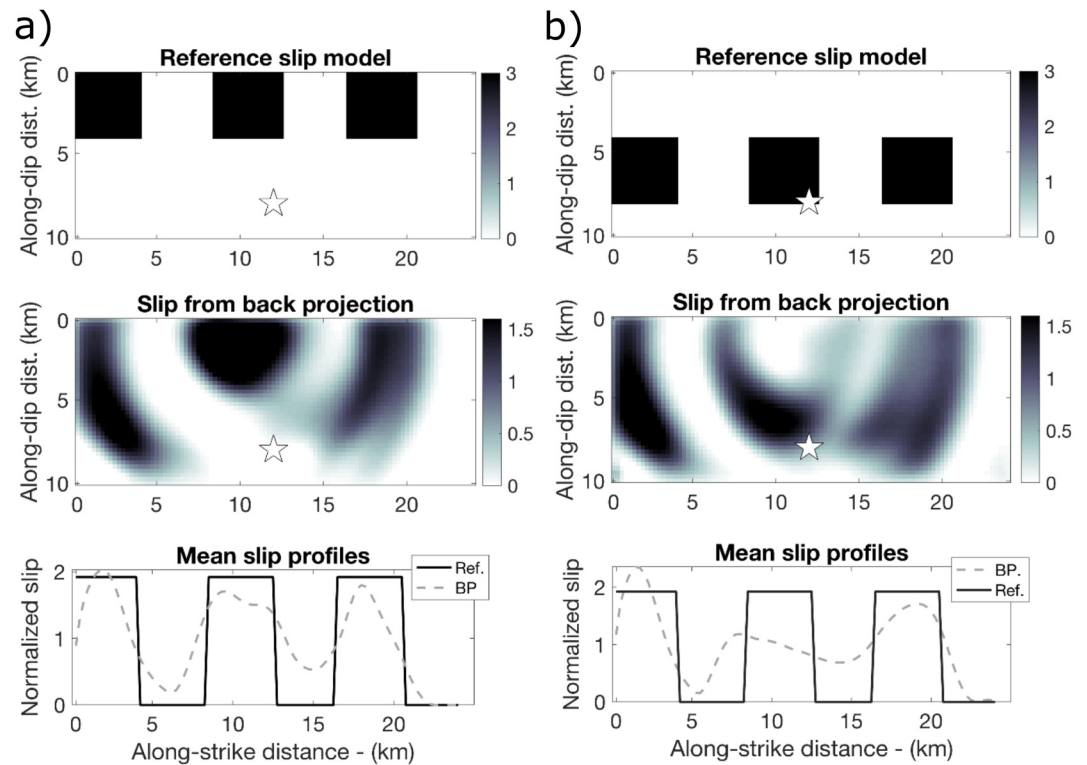
Figure 10. Resolution test of the isochrones backprojection technique for the position of the slip patches located above the hypocenter (a) and for the slip patches located at 5–10 km each side of the hypocenter (b). Synthetic Apparent Source Time Functions (ASTFs) are generated using two reference slip models (top) at the stations for which ASTFs have been inferred from the seismological data (represented on Figure 1 in yellow and green), assuming a rupture velocity of 2 km/s and a hypocenter at 7.8 km depth. Middle and bottom figures show the inferred slip maps and slip profiles averaged over the fault dip, respectively.

Information S1) but provides smoother slip with slightly larger rupture area and smaller maximum slip. We attribute this feature to the "smearing" effect (Figure 10). This also explains why the source function resulting from the backprojection kinematic model has slightly longer duration (Figure S5 in Supporting Information S1). As such, the backprojection method provides fast estimates of the rupture parameters that are fairly consistent with the Bayesian inversion results.
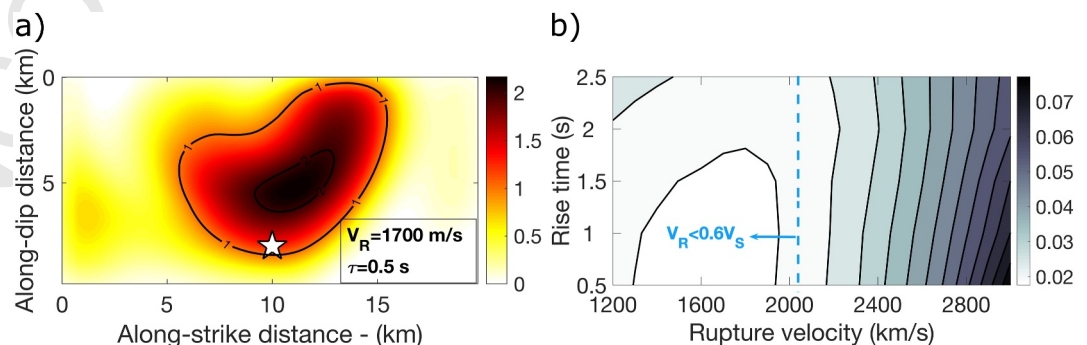
Figure 11. Results from the isochrone backprojection technique for the $M_w 6.4$ Petrinja earthquake. (a) Slip map obtained from the isochrone backprojection of Apparent Source Time Functions (ASTFs), assuming a hypocenter at ~8 km. The minimum misfit between synthetic and observed ASTFs is obtained for a rupture velocity of 1.7 km/s and a rise time of 0.5 s. (b) Misfit value as a function of rise time and rupture velocity. The first contour line denotes misfit values equal to 110% of the minimum misfit value.

4. Discussion

4.1. Large Stress Drop

The stress drop value of 24 MPa inferred for the Petrinja earthquake from the corner frequency analysis of *P*-waves exceeds the average value of 6 MPa expected for shallow intraplate earthquakes (Allmann & Shearer, 2009). It also exceeds the stress drop values reported for the 3 mainshocks of the 2016 Central Italy seismic sequence (M_W6.0 Amatrice, M_W5.9 Visso, and M_W6.5 Norcia earthquakes), which range from 2 to 6 MPa (Calderoni & Abercrombie, 2023). For a given moment magnitude, stress drop is inversely proportional to $S^{3/2}$, where *S* represents the rupture area (*S*) (e.g., Eshelby, 1957; Kanamori & Anderson, 1975). As such, the large stress drop of the Petrinja earthquake is also supported by the small inferred rupture length and rupture area for a M_W6.4 earthquake. The empirical relationships by Wells and Coppersmith (1994), Leonard et al. (2010), and Thingbaijam et al. (2017) indicate average rupture lengths of 25 km, 16 km, and 26 km and rupture areas of 220 km², 250 km², and 350 km², respectively. Our inferred rupture length and rupture area are however ∼7 km and 40 km² from the Bayesian inversion, in agreement with the previously published slip models (Section 3.1.2). Assuming a circular crack model (Eshelby, 1957), the stress drop is given by $\Delta\tau = 7/16 M_0 (\pi/S)^{3/2}$, leading to a value of 50 MPa. Here, *S* is determined as the area with slip above 1 m, which is also consistent with the slip image trimming procedure proposed by Somerville et al. (1999). Considering *S* as the surface, with slip larger than 5% or 10% of the maximum slip, would lead to stress drop values of 26 and 35 MPa, respectively. This is consistent with the stress drop value of 27 MPa proposed by Xiong et al. (2021). Finally, stress drop is inversely proportional to $(TV_R)^3$, where *T* denotes the duration of the source function (e.g., Chounet et al., 2018). The average duration of 5–6 s inferred for Petrinja is only slightly smaller than the average value of 8 s obtained by Courboulex et al. (2016) for shallow earthquakes from the SCARDEC database of source functions (Vallée & Douet, 2016), but combined with the slow rupture propagation, this is consistent with a large stress drop. It is important to note that stress drop estimates strongly varies with the considered methodology (e.g., Abercrombie, 2021; Gallovič & Valentová, 2020; Kaneko & Shearer, 2015; Noda et al., 2013). For instance, Kaneko and Shearer (2015) computed stress drop using various point source models. While the classical assumption of a symmetric circular crack of Madariaga (1976) results in a stress drop of 24 MPa (*k* = 0.32 in Equation 3), assuming a slower rupture velocity of $0.6V_S$ and an asymmetric crack model, which is more consistent with our inverted kinematic rupture model, would result in a stress drop of 83 MPa. We tested whether shorter $T_S - T_P$ windows introduce bias. With a minimum duration of 9 s and a median of 34 s, stress drop calculations remained consistent, both when using data with $T_S - T_P > 30$ s and when including shorter windows. Thus, based on the above-mentioned considerations, both corner frequency and kinematic model analyses point to a large stress drop, due to a concentrated slip distribution.

4.2. Interpretation of Large Stress Drop and Slow Rupture Propagation

The 2020 Petrinja earthquake is a rare example of shallow rupture with large stress drop. The large stress drop suggests that the fault strength was large enough to allow strong accumulation and then release of stress. Such conditions are favored by geometric complexity and strength heterogeneity of the fault (e.g., Fang & Dunham, 2013; Madariaga, 1979; Zielke et al., 2017), features expected for an immature and complex fault system like the Petrinja-Pokupsko fault (Xiong et al., 2021). The long recurrence interval of large earthquakes on this fault, characterized by slip rate estimates of 0.1–0.6 mm/yr (Baize et al., 2022; Basili et al., 2013) could also promote cohesion recovery and increase fault strength (Xu et al., 2023).

Furthermore, the high seismological stress drop is consistent with the small rupture length (∼7 km) and the large maximum slip that probably reached over 5 m at 4–5 km depth. Surface rupture observations indicate maximum surface slip of only 38 cm (Baize et al., 2022), which implies a large shallow slip deficit. Large deficit is also revealed by the slip distribution obtained from geodetic data (Henriquet et al., 2022). Observations of shallow slip deficit are commonly attributed to shallow distributed inelastic deformation in an immature fault context (Dolan & Haravitch, 2014; Fialko et al., 2005; Li et al., 2020; Roten et al., 2017). Shallow coseismic deformation during the Petrinja earthquake may have occurred in a zone of diffuse deformation (or damage zone) a few kilometers wide as revealed by the "flower structure" of the Petrinja-Pokupsko fault and by the segmented coseismic rupture observed at the surface (Baize et al., 2022). The broad extent of the aftershock distribution of the Petrinja seismic sequence (Figure 1) is also a characteristic of immature fault systems and distributed coseismic deformation (Perrin et al., 2021).

Another unusual characteristic of the 2020 Petrinja earthquake is its slow rupture. The rupture propagated at a speed of about $0.5V_S$, while commonly reported rupture speeds range between ~$0.6V_S$ and ~$0.9V_S$ (e.g., Heaton, 1990; Somerville et al., 1999). The database of rupture velocity values computed by Chounet et al. (2018) for 100 earthquakes of magnitude larger than 5.5 indicate that ~80% of the ruptures propagate at a speed larger than 1,800 m/s, which is the mean inferred from our Bayesian inversion. Low rupture speeds have been observed for other continental intraplate earthquakes generally on immature faults structures with complex geometries, including the 1999 Hector Mine (Kaverina, 2002), the 2012 $M_W5.8$ and $M_W6.0$ Emilia (Causse et al., 2017; Convertito et al., 2021), the 2016 Tottori (Ross et al., 2018), the 2020 Elazig (Pousse-Beltran et al., 2020), the 2021 Ridgecrest (Goldberg et al., 2020; Liu et al., 2019) and the 2021 Yangbi, Yunnan (Gong et al., 2022) earthquakes. Slow rupture implies strong energy dissipation in the fault zone near the crack tip and in the surrounding rock (e.g., Cocco et al., 2023; Freund, 1972). Processes of energy dissipation during faulting include off-fault cracking (Andrews, 2005; Rice et al., 2005) and thermal processes such as melting and thermal-pressurization (Rice, 2006). Nonelastic dynamic simulations shows that off-fault cracking reduces rupture velocity (Andrews, 2005; Gabriel et al., 2013). It is likely that off-fault cracking in the immature and segmented Pertinja-Pokupsko fault zone strongly contributed to the low rupture velocity.

In terms of earthquake energy partitioning, slow rupture propagation implies that a relatively small amount of the available energy is radiated as seismic waves (*i.e.*, lower radiation efficiency) (Freund, 1972; Kanamori & Rivera, 2006; Venkataraman & Kanamori, 2004). An interesting question is whether low rupture velocity and radiation efficiency together with a large stress drop are common features of earthquake ruptures. In other words, does the energy dissipated during the rupture process increase with stress drop? Such properties have been reported for the 2016 $M_W6.2$ Tottori earthquake ($V_R \sim 0.5–0.6V_S$, $\eta_R \sim 7\%$, $\Delta\tau \sim 20–30$ MPa) (Ross et al., 2018). At a global scale, Chounet et al. (2018) documented rupture properties of 96 shallow earthquakes with magnitude M_W from 6 to 9 and show that rupture velocity and stress drop are anticorrelated, supporting slower rupture propagation when stress drop is large. Another example where this behavior is explicitly mentioned is the 2003 Big Bear sequence for events with magnitude 3–4 (Tan & Helmberger, 2010). Anticorrelation between rupture velocity and stress drop was initially proposed by Causse and Song (2015) by combinating observations of the variability of source properties and high-frequency ground motion. Dynamic rupture simulations and laboratory experiments conducted in homogeneous media generally indicate a positive correlation between rupture velocity and stress drop (e.g., Andrews, 1976; Dong et al., 2023; Guatteri, 2004). However, dynamic simulations including off-fault plasticity show that this trend can be reversed, depending on the orientation of the maximum compressive stress angle with respect to fault strike (denoted ψ) (Gabriel et al., 2013). Such a behavior is observed for ψ values larger than 50°. In this case, off-fault energy dissipation is strongly boosted as stress drop is increased. Stress orientations based on focal mechanism in the Petrinja region oscillate around the N–S axis (Baize et al., 2022; Herak et al., 2009), in agreement with geodetic velocity field (Métois et al., 2015). This leads to ψ values of ~60–65° for the Petrinja-Pokupsko fault - consistently with the transpressive faulting regime, supporting strong off-fault energy dissipation enhanced by the large stress drop. In other words, high stress drop may be counterproductive for earthquake rupture because energy dissipation in the surrounding material becomes catastrophic, which in turn makes the rupture on the main fault less efficient. Further studies should investigate if large stress drop and slow rupture velocity are observed in similar tectonic environments. Another interpretation is that rupture may appear to be slow because it is confined to a small fault zone due to the geometric complexity and strength heterogeneity of the immature fault, conditions also responsible for high stress drop. This is an interesting question for future rupture dynamic studies.

Finally, an important question for seismic hazard assessment is the implication of such rupture properties on ground motion. Unfortunately, the strong ground motion of the Petrinja earthquake was not recorded at less than ~50 km from the source. Radiguet et al. (2009) observed that ground motions generated on immature faults are ~1.5 time larger than the ones on mature faults. The large seismological stress drop that we obtain for the Petrinja-Pokupsko immature fault (~25 MPa) suggests that the high-frequency ground motion was high, at least in the region far from the source (e.g., Cotton et al., 2013). Near-fault ground motion is however highly sensitive to the rupture velocity (e.g., Bouchon et al., 2006; Fayjaloun et al., 2020). Further studies are necessary to quantify the near-fault ground motion and analyze the impact of the large stress drop and slow rupture propagation.

5. Conclusions

In this study, we analyzed the rupture process of the 29 December 2020, $M_W6.4$ earthquake that struck the wider Petrinja area (Croatia) using seismological data from more than 80 broadband stations. We used an EGF deconvolution method to compute stress drop and to derive ASTFs. Using two separate methods, Bayesian inversion of ASTFs and backprojection of ASTFs on isochrones, we derived a kinematic rupture model. Both methods revealed a relatively small rupture length of less than 10 km and a significant maximum slip of more than 5 m, consistent with the large Brune's stress drop (∼25 MPa) and the relatively short rupture duration (∼5 s). Moreover, the two methods unambiguously point to a slow rupture velocity of ∼50% of the shear wave velocity, ranging from 1,420 m/s based on kinematic inversion to 1,700 m/s obtained through isochrone backprojection.

The Petrinja earthquake is a rare example of shallow event with large stress drop. The large stress drop may have been favored by the complexity and heterogeneity of the fault geometry, which are typical features of immature fault systems. While dynamic rupture simulations and laboratory experiments commonly indicate that rupture velocity increases with stress drop, the rupture propagation during the Petrinja rupture was particularly slow. Such particular behavior is supported by anticorrelation between stress drop and rupture velocity observed in set of rupture models (Causse et al., 2015; Chounet et al., 2018). Physically, the slow rupture velocity may be explained by a particularly strong energy dissipation in off-fault cracking, enhanced by the large stress drop, as reported in some dynamic rupture simulations including off-fault plasticity. Whether or not large stress drop and slow rupture propagation are common features of earthquakes in immature intraplate setting prompts further investigations. An important question for seismic hazard assessment is also how these particular rupture properties affect near-fault ground motion.

Data Availability Statement

Seismological data across Europe are available in open-access at the Observatories and Research Facilities for European Seismology (ORFEUS) data center. They have been downloaded using webservices of the European Integrated Data Archive (EIDA, Strollo et al., 2021) and ObsPy codes. The Croatian data that support the findings of this study are available from Žilić et al. (2024) and from Croatian Seismograph Network (CR; University of Zagreb, 2001).

References

Abercrombie, R. E. (2015). Investigating uncertainties in empirical Green's function analysis of earthquake source parameters. *Journal of Geophysical Research: Solid Earth*, *120*(6), 4263–4277. https://doi.org/10.1002/2015jb011984

Abercrombie, R. E. (2021). Resolution and uncertainties in estimates of earthquake stress drop and energy release. *Philosophical Transactions of the Royal Society A*, *379*(2196), 20200131. https://doi.org/10.1098/rsta.2020.0131

Abercrombie, R. E., Bannister, S., Ristau, J., & Doser, D. (2016). Variability of earthquake stress drop in a subduction setting, the Hikurangi Margin, New Zealand. *Geophysical Journal International*, *208*(1), 306–320. https://doi.org/10.1093/gji/ggw393

Aki, K. (1967). Scaling law of seismic spectrum. *Journal of Geophysical Research*, *72*(4), 1217–1231. https://doi.org/10.1029/jz072i004p01217

Allmann, B. P., & Shearer, P. M. (2009). Global variations of stress drop for moderate to large earthquakes. *Journal of Geophysical Research*, *114*(B1). https://doi.org/10.1029/2008jb005821

Anderson, H., & Jackson, J. (1987). Active tectonics of the Adriatic region. *Geophysical Journal International*, *91*(3), 937–983. https://doi.org/10.1111/j.1365-246x.1987.tb01675.x

Andrews, D. J. (1976). Rupture propagation with finite stress in antiplane strain. *Journal of Geophysical Research*, *81*(20), 3575–3582. https://doi.org/10.1029/jb081i020p03575

Andrews, D. J. (2005). Rupture dynamics with energy loss outside the slip zone. *Journal of Geophysical Research*, *110*(B1). https://doi.org/10.1029/2004jb003191

Baize, S., Amoroso, S., Belić, N., Benedetti, L., Boncio, P., Budić, M., et al. (2022). Environmental effects and seismogenic source characterization of the December 2020 earthquake sequence near Petrinja, Croatia. *Geophysical Journal International*, *230*(2), 1394–1418. https://doi.org/10.1093/gji/ggac123

Battaglia, M., Murray, M. H., Serpelloni, E., & Bürgmann, R. (2004). The Adriatic region: An independent microplate within the Africa-Eurasia collision zone. *Geophysical Research Letters*, *31*(9). https://doi.org/10.1029/2004gl019723

B.C.I.S. (1972). *Tables des temp de propagation des ondes séismiques (Hodochrones) pour la région des Balkans*. Manuel d'utilisation, Bureau Central International de Séismologie.

Beroza, G. C., & Spudich, P. (1988). Linearized inversion for fault rupture behavior: Application to the 1984 Morgan Hill, California, earthquake. *Journal of Geophysical Research*, *93*(B6), 6275–6296. https://doi.org/10.1029/jb093ib06p06275

Bertero, M., Bindi, D., Boccacci, P., Cattaneo, M., Eva, C., & Lanza, V. (1997). Application of the projected Landweber method to the estimation of the source time function in seismology. *Inverse Problems*, *13*(2), 465–486. https://doi.org/10.1088/0266-5611/13/2/017

Bouchon, M., Hatzfeld, D., Jackson, J. A., & Haghshenas, E. (2006). Some insight on why Bam (Iran) was destroyed by an earthquake of relatively moderate size. *Geophysical Research Letters*, *33*(9). https://doi.org/10.1029/2006gl025906

Brune, J. N. (1970). Tectonic stress and the spectra of seismic shear waves from earthquakes. *Journal of Geophysical Research*, *75*(26), 4997–5009. https://doi.org/10.1029/jb075i026p04997

Calais, E., Nocquet, J.-M., Jouanne, F., & Tardy, M. (2002). Current strain regime in the Western Alps from continuous Global Positioning System measurements, 1996–2001. *Geology*, *30*(7), 651. https://doi.org/10.1130/0091-7613(2002)030<0651:csritw>2.0.co;2

Calderoni, G., & Abercrombie, R. E. (2023). Investigating spectral estimates of stress drop for small to moderate earthquakes with heterogeneous slip distribution: Examples from the 2016-2017 Amatrice earthquake sequence. *Journal of Geophysical Research: Solid Earth*, *128*(6), e2022JB025022. https://doi.org/10.1029/2022JB025022

Causse, M., Cornou, C., Maufroy, E., Grasso, J.-R., Baillet, L., & El Haber, E. (2021). Exceptional ground motion during the shallow Mw 4.9 2019 Le Teil earthquake, France. *Communications Earth & Environment*, *2*(1), 14. https://doi.org/10.1038/s43247-020-00089-0

Causse, M., Cultrera, G., Moreau, L., Herrero, A., Schiappapietra, E., & Courboulex, F. (2017). Bayesian rupture imaging in a complex medium: The 29 May 2012 Emilia, Northern Italy, earthquake. *Geophysical Research Letters*, *44*(15), 7783–7792. https://doi.org/10.1002/2017gl074698

Causse, M., & Song, S. G. (2015). Are stress drop and rupture velocity of earthquakes independent? Insight from observed ground motion variability. *Geophysical Research Letters*, *42*(18), 7383–7389. https://doi.org/10.1002/2015gl064793

Chounet, A., Vallée, M., Causse, M., & Courboulex, F. (2018). Global catalog of earthquake rupture velocities shows anticorrelation between stress drop and rupture velocity. *Tectonophysics*, *733*, 148–158. https://doi.org/10.1016/j.tecto.2017.11.005

Cocco, M., Aretusini, S., Cornelio, C., Nielsen, S. B., Spagnuolo, E., Tinti, E., & Di Toro, G. (2023). Fracture energy and breakdown work during earthquakes. *Annual Review of Earth and Planetary Sciences*, *51*(1), 217–252. https://doi.org/10.1146/annurev-earth-071822-100304

Convertito, V., Pino, N. A., & Piccinini, D. (2021). Concentrated slip and low rupture velocity for the may 20, 2012, MW 5.8, Po plain (northern Italy) earthquake revealed from the analysis of source time functions. *Journal of Geophysical Research: Solid Earth*, *126*(1). https://doi.org/10.1029/2019jb019154

Cotton, F., Archuleta, R., & Causse, M. (2013). What is sigma of the stress drop? *Seismological Research Letters*, *84*(1), 42–48. https://doi.org/10.1785/0220120087

Courboulex, F., Vallée, M., Causse, M., & Chounet, A. (2016). Stress-Drop variability of shallow earthquakes extracted from a global database of source time functions. *Seismological Research Letters*, *87*(4), 912–918. https://doi.org/10.1785/0220150283

Dolan, J. F., & Haravitch, B. D. (2014). How well do surface slip measurements track slip at depth in large strike-slip earthquakes? The importance of fault structural maturity in controlling on-fault slip versus off-fault surface deformation. *Earth and Planetary Science Letters*, *388*, 38–47. https://doi.org/10.1016/j.epsl.2013.11.043

Dong, P., Xia, K., Xu, Y., Elsworth, D., & Ampuero, J.-P. (2023). Laboratory earthquakes decipher control and stability of rupture speeds. *Nature Communications*, *14*(1), 2427. https://doi.org/10.1038/s41467-023-38137-w

Eshelby, J. D. (1957). The determination of the elastic field of an ellipsoidal inclusion, and related problems. *Proceedings of the Royal Society of London. Series A. Mathematical and Physical Sciences*, *241*(1226), 376–396. https://doi.org/10.1098/rspa.1957.0133

Fang, Z., & Dunham, E. M. (2013). Additional shear resistance from fault roughness and stress levels on geometrically complex faults. *Journal of Geophysical Research: Solid Earth*, *118*(7), 3642–3654. https://doi.org/10.1002/jgrb.50262

Fayjaloun, R., Causse, M., Cornou, C., Voisin, C., & Song, S. G. (2020). Sensitivity of high-frequency ground motion to kinematic source parameters. *Pure and Applied Geophysics*, *177*(5), 1947–1967. https://doi.org/10.1007/s00024-019-02195-3

Festa, G., & Zollo, A. (2006). Fault slip and rupture velocity inversion by isochrone backprojection. *Geophysical Journal International*, *166*(2), 745–756. https://doi.org/10.1111/j.1365-246x.2006.03045.x

Fialko, Y., Sandwell, D., Simons, M., & Rosen, P. (2005). Three-dimensional deformation caused by the Bam, Iran, earthquake and the origin of shallow slip deficit. *Nature*, *435*(7040), 295–299. https://doi.org/10.1038/nature03425

Freund, L. B. (1972). Crack propagation in an elastic solid subjected to general loading—I. Constant rate of extension. *Journal of the Mechanics and Physics of Solids*, *20*(3), 129–140. https://doi.org/10.1016/0022-5096(72)90006-3

Gabriel, A.-a., Ampuero, J.-p., Dalguer, L. A., & Mai, P. M. (2013). Source properties of dynamic rupture pulses with off-fault plasticity. *Journal of Geophysical Research: Solid Earth*, *118*(8), 4117–4126. https://doi.org/10.1002/jgrb.50213

Gallovič, F., & Valentová, Ľ. (2020). Earthquake stress drops from dynamic rupture simulations constrained by observed ground motions. *Geophysical Research Letters*, *47*(4), e2019GL085880. https://doi.org/10.1029/2019gl085880

Goldberg, D., Melgar, D., Thomas, A., Sahakian, V., Xu, X., Geng, J., & Crowell, B. (2020). Complex rupture of an immature fault zone: A simultaneous kinematic model of the 2019 Ridgecrest, CA earthquakes. *California Digital Library (CDL)*. https://doi.org/10.31223/osf.io/s79bk

Gong, W., Ye, L., Qiu, Y., Lay, T., & Kanamori, H. (2022). Rupture directivity of the 2021MW6.0 Yangbi, Yunnan earthquake. *Journal of Geophysical Research: Solid Earth*, *127*(9). https://doi.org/10.1029/2022jb024321

Guatteri, M. (2004). A pseudo-dynamic approximation to dynamic rupture models for strong ground motion prediction. *Bulletin of the Seismological Society of America*, *94*(6), 2051–2063. https://doi.org/10.1785/0120040037

Gusev, A. A., & Chebrov, D. (2019). On scaling of earthquake rise-time estimates. *Bulletin of the Seismological Society of America*, *109*(6), 2741–2745. https://doi.org/10.1785/0120180214

Hallo, M., & Gallovič, F. (2020). Bayesian self-adapting fault slip inversion with green's functions uncertainty and application on the 2016 Mw7.1 Kumamoto Earthquake. *Journal of Geophysical Research: Solid Earth*, *125*(3). https://doi.org/10.1029/2019jb018703

Hartzell, S. H. (1978). Earthquake aftershocks as Green's functions. *Geophysical Research Letters*, *5*(1), 1–4. https://doi.org/10.1029/gl005i001p00001

Heaton, T. H. (1990). Evidence for and implications of self-healing pulses of slip in earthquake rupture. *Physics of the Earth and Planetary Interiors*, *64*(1), 1–20. https://doi.org/10.1016/0031-9201(90)90002-f

Henriquet, M., Kordic, B., Métois, M., Lasserre, C., Baize, S., Benedetti, L., et al. (2022). Rapid remeasure of dense civilian networks as a game-changer tool for surface deformation monitoring: The case study of the Mw 6.4 2020 Petrinja Earthquake, Croatia. *Geophysical Research Letters*, *49*(24). https://doi.org/10.1029/2022gl100166

Herak, D., & Herak, M. (2010). The kupa valley (Croatia) earthquake of 8 october 1909--100 years later. *Seismological Research Letters*, *81*(1), 30–36. https://doi.org/10.1785/gssrl.81.1.30

Herak, D., Herak, M., & Tomljenović, B. (2009). Seismicity and earthquake focal mechanisms in North-Western Croatia. *Tectonophysics*, *465*(1–4), 212–220. https://doi.org/10.1016/j.tecto.2008.12.005

Herak, M. (1989). HYPOSEARCH—An earthquake location program. *Computers & Geosciences*, *15*(7), 1157–1162. https://doi.org/10.1016/0098-3004(89)90127-1

Herak, M., & Herak, D. (2023). Properties of the Petrinja (Croatia) earthquake sequence of 2020–2021 – Results of seismological research for the first six months of activity. *Tectonophysics*, *858*, 229885. https://doi.org/10.1016/j.tecto.2023.229885

Herak, M., Herak, D., & Markušić, S. (1996). Revision of the earthquake catalogue and seismicity of Croatia, 1908–1992. *Terra Nova*, *8*(1), 86–94. https://doi.org/10.1111/j.1365-3121.1996.tb00728.x

Holmgren, J. M., Atkinson, G. M., & Ghofrani, H. (2019). Stress drops and directivity of induced earthquakes in the western Canada sedimentary basin. *Bulletin of the Seismological Society of America*, *109*(5), 1635–1652. https://doi.org/10.1785/0120190035

Houston, H. (2001). Influence of depth, focal mechanism, and tectonic setting on the shape and duration of earthquake source time functions. *Journal of Geophysical Research*, *106*(B6), 11137–11150. https://doi.org/10.1029/2000jb900468

Kanamori, H., & Anderson, D. L. (1975). Theoretical basis of some empirical relations in seismology. *Bulletin of the Seismological Society of America*, *65*, 1073–1095.

Kanamori, H., & Rivera, L. (2006). Energy partitioning during an earthquake. In *Earthquakes: Radiated energy and the physics of faulting* (pp. 3–13). American Geophysical Union. https://doi.org/10.1029/170gm03

Kane, D. L., Prieto, G. A., Vernon, F. L., & Shearer, P. M. (2011). Quantifying seismic source parameter uncertainties. *Bulletin of the Seismological Society of America*, *101*(2), 535–543. https://doi.org/10.1785/0120100166

Kaneko, Y., & Shearer, P. M. (2015). Variability of seismic source spectra, estimated stress drop, and radiated energy, derived from cohesive-zone models of symmetrical and asymmetrical circular and elliptical ruptures. *Journal of Geophysical Research: Solid Earth*, *120*(2), 1053–1079. https://doi.org/10.1002/2014jb011642

Kastelic, V., Atzori, S., Carafa, M. M. C., Marin Govorčin, M., Herak, D., Herak, M., et al. (2021). *Petrinja seismogenic source and its 2020-2021 earthquake sequence (central Croatia)*. Copernicus GmbH. https://doi.org/10.5194/egusphere-egu21-16585

Kaverina, A. (2002). The combined inversion of seismic and geodetic data for the source process of the 16 october 1999 Mw 7.1 Hector Mine, California, earthquake. *Bulletin of the Seismological Society of America*, *92*(4), 1266–1280. https://doi.org/10.1785/0120000907

Király-Proag, E., Satriano, C., Bernard, P., & Wiemer, S. (2019). Rupture process of the Mw 3.3 Earthquake in the St. Gallen 2013 Geothermal Reservoir, Switzerland. *Geophysical Research Letters*, *46*(14), 7990–7999. https://doi.org/10.1029/2019gl082911

Kirkpatrick, S., Gelatt, C. D., Jr., & Vecchi, M. P. (1983). Optimization by simulated annealing. *Science*, *220*(4598), 671–680. https://doi.org/10.1126/science.220.4598.671

Lay, T., & Wallace, T. C. (1995). *Modern global seismology*. Elsevier.

Leonard, M. (2010). Earthquake fault scaling: Self-consistent relating of rupture length, width, average displacement, and moment release. *Bulletin of the Seismological Society of America*, *100*(5A), 1971–1988. https://doi.org/10.1785/0120090189

Li, Y., Bürgmann, R., & Zhao, B. (2020). Evidence of fault immaturity from shallow slip deficit and lack of postseismic deformation of the 2017 Mw 6.5 Jiuzhaigou Earthquake. *Bulletin of the Seismological Society of America*, *110*(1), 154–165. https://doi.org/10.1785/0120190162

Liu, C., Lay, T., Brodsky, E. E., Dascher-Cousineau, K., & Xiong, X. (2019). Coseismic rupture process of the large 2019 ridgecrest earthquakes from joint inversion of geodetic and seismological observations. *Geophysical Research Letters*, *46*(21), 11820–11829. https://doi.org/10.1029/2019gl084949

Madariaga, R. (1976). Dynamics of an expanding circular fault. *Bulletin of the Seismological Society of America*, *66*(3), 639–666. https://doi.org/10.1785/bssa0660030639

Madariaga, R. (1979). On the relation between seismic moment and stress drop in the presence of stress and strength heterogeneity. *Journal of Geophysical Research*, *84*(B5), 2243–2250. https://doi.org/10.1029/jb084ib05p02243

Markušić, S., Stanko, D., Penava, D., Ivančić, I., Bjelotomić Oršulić, O., Korbar, T., & Sarhosis, V. (2021). Destructive M6.2 Petrinja Earthquake (Croatia) in 2020—Preliminary multidisciplinary research. *Remote Sensing*, *13*(6), 1095. https://doi.org/10.3390/rs13061095

McGarr, A., & Fletcher, J. B. (2003). Maximum slip in earthquake fault zones, apparent stress, and stick-slip friction. *Bulletin of the Seismological Society of America*, *93*(6), 2355–2362. https://doi.org/10.1785/0120030037

Meng, H., McGuire, J. J., & Ben-Zion, Y. (2020). Semiautomated estimates of directivity and related source properties of small to moderate Southern California earthquakes using second seismic moments. *Journal of Geophysical Research: Solid Earth*, *125*(4), e2019JB018566. https://doi.org/10.1029/2019jb018566

Métois, M., D'Agostino, N., Avallone, A., Chamot-Rooke, N., Rabaute, A., Duni, L., et al. (2015). Insights on continental collisional processes from GPS data: Dynamics of the peri-Adriatic belts. *Journal of Geophysical Research: Solid Earth*, *120*(12), 8701–8719. https://doi.org/10.1002/2015jb012023

Metropolis, N., Rosenbluth, A. W., Rosenbluth, M. N., Teller, A. H., & Teller, E. (1953). Equation of state calculations by fast computing machines. *The Journal of Chemical Physics*, *21*(6), 1087–1092. https://doi.org/10.1063/1.1699114

Miranda, E. B., Bijelic, S., Arbanas, N., Bartolac, Ž., Jagodnik, M., Lazarević, V., et al. (2021). Joint reconnaissance report (JRR). In *StEER-EERI: PETRINJA, CROATIA DECEMBER 29, 2020, Mw 6.4 EARTHQUAKE*.

Moreau, L., Hunter, A., Velichko, A., & Wilcox, P. (2014). 3-D reconstruction of sub-wavelength scatterers from the measurement of scattered fields in elastic waveguides. *IEEE Transactions on Ultrasonics, Ferroelectrics, and Frequency Control*, *61*(11), 1864–1879. https://doi.org/10.1109/tuffc.2014.006619

Mueller, C. S. (1985). Source pulse enhancement by deconvolution of an empirical Green's function. *Geophysical Research Letters*, *12*(1), 33–36. https://doi.org/10.1029/gl012i001p00033

Onwuemeka, J., Liu, Y., & Harrington, R. M. (2018). Earthquake stress drop in the Charlevoix Seismic Zone, Eastern Canada. *Geophysical Research Letters*, *45*(22). https://doi.org/10.1029/2018gl079382

Perrin, C., Waldhauser, F., & Scholz, C. H. (2021). The shear deformation zone and the smoothing of faults with displacement. *Journal of Geophysical Research: Solid Earth*, *126*(5). https://doi.org/10.1029/2020jb020447

Podvin, P., & Lecomte, I. (1991). Finite difference computation of traveltimes in very contrasted velocity models: A massively parallel approach and its associated tools. *Geophysical Journal International*, *105*(1), 271–284. https://doi.org/10.1111/j.1365-246x.1991.tb03461.x

Pousse-Beltran, L., Nissen, E., Bergman, E. A., Cambaz, M. D., Gaudreau, É., Karasözen, E., & Tan, F. (2020). The 2020 mw 6.8 Elazığ (Turkey) earthquake reveals rupture behavior of the East Anatolian fault. *Geophysical Research Letters*, *47*(13). https://doi.org/10.1029/2020gl088136

Radiguet, M., Cotton, F., Manighetti, I., Campillo, M., & Douglas, J. (2009). Dependency of near-field ground motions on the structural maturity of the ruptured faults. *Bulletin of the Seismological Society of America*, *99*(4), 2572–2581. https://doi.org/10.1785/0120080340

Rice, J. R. (2006). Heating and weakening of faults during earthquake slip. *Journal of Geophysical Research*, *111*(B5). https://doi.org/10.1029/2005jb004006

Rice, J. R., Sammis, C. G., & Parsons, R. (2005). Off-Fault secondary failure induced by a dynamic slip pulse. *Bulletin of the Seismological Society of America*, *95*(1), 109–134. https://doi.org/10.1785/0120030166

Ross, Z. E., Kanamori, H., Hauksson, E., & Aso, N. (2018). Dissipative intraplate faulting during the 2016 Mw 6.2 Tottori, Japan Earthquake. *Journal of Geophysical Research: Solid Earth*, *123*(2), 1631–1642. https://doi.org/10.1002/2017jb015077

Roten, D., Olsen, K. B., & Day, S. M. (2017). Off-fault deformations and shallow slip deficit from dynamic rupture simulations with fault zone plasticity. *Geophysical Research Letters*, *44*(15), 7733–7742. https://doi.org/10.1002/2017gl074323

Shearer, P. M., Abercrombie, R. E., Trugman, D. T., & Wang, W. (2019). Comparing EGF methods for estimating corner frequency and stress drop from P wave spectra. *Journal of Geophysical Research: Solid Earth*, *124*(4), 3966–3986. https://doi.org/10.1029/2018jb016957

Strollo, A., Cambaz, D., Clinton, J., Danecek, P., Evangelidis, C. P., Marmureanu, A., et al. (2021). EIDA: The European integrated data archive and service infrastructure within ORFEUS. *Seismological Society of America*, *92*(3), 1788–1795. https://doi.org/10.1785/0220200413

Tan, Y., & Helmberger, D. (2010). Rupture directivity characteristics of the 2003 big bear sequence. *Bulletin of the Seismological Society of America*, *100*(3), 1089–1106. https://doi.org/10.1785/0120090074

Thingbaijam, K. K. S., Martin Mai, P., & Goda, K. (2017). New empirical earthquake source-scaling laws. *Bulletin of the Seismological Society of America*, *107*(5), 2225–2246. https://doi.org/10.1785/0120170017

Uchide, T., & Song, S. G. (2018). Fault rupture model of the 2016 Gyeongju, South Korea, earthquake and its implication for the underground fault system. *Geophysical Research Letters*, *45*(5), 2257–2264. https://doi.org/10.1002/2017gl076960

University of Zagreb. (2001). Croatian Seismograph network [Dataset]. *International Federation of Digital Seismograph Networks*. https://doi.org/10.7914/SN/CR

Ustaszewski, K., Kounov, A., Schmid, S. M., Schaltegger, U., Krenn, E., Frank, W., & Fügenschuh, B. (2010). Evolution of the Adria-Europe plate boundary in the northern Dinarides: From continent-continent collision to back-arc extension. *Tectonics*, *29*(6). https://doi.org/10.1029/2010tc002668

Ustaszewski, K., Schmid, S. M., Fügenschuh, B., Tischler, M., Kissling, E., & Spakman, W. (2008). A map-view restoration of the Alpine-Carpathian-Dinaridic system for the Early Miocene. *Swiss Journal of Geosciences*, *101*(S1), 273–294. https://doi.org/10.1007/s00015-008-1288-7

Vallée, M. (2004). Stabilizing the empirical green function analysis: Development of the projected landweber method. *Bulletin of the Seismological Society of America*, *94*(2), 394–409. https://doi.org/10.1785/0120030017

Vallée, M., & Douet, V. (2016). A new database of source time functions (STFs) extracted from the SCARDEC method. *Physics of the Earth and Planetary Interiors*, *257*, 149–157. https://doi.org/10.1016/j.pepi.2016.05.012

Venkataraman, A., & Kanamori, H. (2004). Observational constraints on the fracture energy of subduction zone earthquakes. *Journal of Geophysical Research*, *109*(B5). https://doi.org/10.1029/2003jb002549

Viegas, G., Abercrombie, R. E., & Kim, W. (2010). The 2002 M5 Au Sable Forks, NY, earthquake sequence: Source scaling relationships and energy budget. *Journal of Geophysical Research*, *115*(B7). https://doi.org/10.1029/2009jb006799

Wells, D. L., & Coppersmith, K. J. (1994). New empirical relationships among magnitude, rupture length, rupture width, rupture area, and surface displacement. *Bulletin of the Seismological Society of America*, *84*(4), 974–1002. https://doi.org/10.1785/bssa0840040974

Xiong, W., Yu, P., Chen, W., Liu, G., Zhao, B., Nie, Z., & Qiao, X. (2021). The 2020Mw 6.4 Petrinja earthquake: A dextral event with large coseismic slip highlights a complex fault system in northwestern Croatia. *Geophysical Journal International*, *228*(3), 1935–1945. https://doi.org/10.1093/gji/ggab440

Xu, S., Fukuyama, E., Yamashita, F., Kawakata, H., Mizoguchi, K., & Takizawa, S. (2023). Fault strength and rupture process controlled by fault surface topography. *Nature Geoscience*, *16*(1), 94–100. https://doi.org/10.1038/s41561-022-01093-z

Zielke, O., Galis, M., & Mai, P. M. (2017). Fault roughness and strength heterogeneity control earthquake size and stress drop. *Geophysical Research Letters*, *44*(2), 777–783. https://doi.org/10.1002/2016gl071700

Žilić, I., Causse, M., Vallée, M., & Markušić, S. (2024). The Petrinja 2020 earthquake sequence - Croatian Seismological Network [Dataset]. *Zenodo*. https://doi.org/10.5281/zenodo.13879616